The massively accreting cluster A2029

(Article begins on next page)

08 November 2024

CrossMark

The Massively Accreting Cluster A2029

Jubee Sohn[1] , Margaret J. Geller[1] , Stephen A. Walker[2] , Ian Dell'Antonio[3], Antonaldo Diaferio[4,5], and Kenneth J. Rines[6]
[1] Smithsonian Astrophysical Observatory, 60 Garden Street, Cambridge, MA 02138, USA
[2] Astrophysics Science Division, X-ray Astrophysics Laboratory, Code 662, NASA Goddard Space Flight Center, Greenbelt, MD 20771, USA
[3] Department of Physics, Brown University, Box 1843, Providence, RI 02912, USA
[4] Università di Torino, Dipartimento di Fisica, Torino, Italy
[5] Istituto Nazionale di Fisica Nucleare (INFN), Sezione di Torino, Torino, Italy
[6] Department of Physics and Astronomy, Western Washington University, Bellingham, WA 98225, USA

Abstract

We explore the structure of galaxy cluster A2029 and its surroundings based on intensive spectroscopy along with X-ray and weak lensing observations. The redshift survey includes 4376 galaxies (1215 spectroscopic cluster members) within 40′ of the cluster center; the redshifts are included here. Two subsystems, A2033 and a southern infalling group (SIG), appear in the infall region based on the spectroscopy, as well as on the weak lensing and X-ray maps. The complete redshift survey of A2029 also identifies at least 12 foreground and background systems (10 are extended X-ray sources) in the A2029 field; we include a census of their properties. The X-ray luminosities (L_X)–velocity dispersions (σ_{cl}) scaling relations for A2029, A2033, SIG, and the foreground/background systems are consistent with the known cluster scaling relations. The combined spectroscopy, weak lensing, and X-ray observations provide a robust measure of the masses of A2029, A2033, and SIG. The total mass of the infalling groups (A2033 and SIG) is ∼60% of the M_{200} of the primary cluster, A2029. Simple dynamical considerations suggest that A2029 will accrete these subsystems in the next few Gyr. In agreement with simulations and other clusters observed in a similar redshift range, the total mass in the A2029 infall region is comparable to the A2029 M_{200} and will mostly be accreted in the long-term future.

Key words: galaxies: clusters: individual (A2029, A2033) – galaxies: distances and redshifts – large-scale structure of universe – surveys – X-rays: galaxies: clusters

Supporting material: machine-readable tables

1. Introduction

Galaxy clusters grow hierarchically through accretion of generally lower-mass systems. More massive clusters typically form later than less massive systems (Neto et al. 2007; Boylan-Kolchin et al. 2009; McBride et al. 2009). Numerical simulations suggest that the mass accretion rate is roughly proportional to the cluster mass: more massive clusters accrete more mass (van den Bosch 2002; Fakhouri & Ma 2008; Fakhouri et al. 2010; Giocoli et al. 2012; De Boni et al. 2016).

Observational estimates of the mass within the infall region of galaxy clusters enable measurement of mass accretion rates (Diaferio & Geller 1997; Rines et al. 2002; De Boni et al. 2016). The measurement of the mass infall rate is challenging because detailed observations covering the cluster outskirts (or infall regions) are required.

Wide field-of-view redshift surveys, X-ray observations, and weak lensing offer complementary views of the infall region of an individual cluster. So far, there are relatively few systems where all of these observations are available. Wide field-of-view redshift surveys (Geller et al. 1999; Reisenegger et al. 2000; Rines et al. 2002) apply the caustic technique (Diaferio & Geller 1997; Diaferio 1999) to estimate the mass in the infall region. Rines et al. (2013) showed that the typical mass in the infall region is comparable with M_{200} ($=(4\pi/3)R_{200}^3 200\rho_{crit}$).

Identification of X-ray-emitting groups in the infall region provides another probe of the future accretion by the cluster. The X-COP project (Eckert et al. 2017) surveys galaxy clusters with very deep *XMM* images to study infalling groups. Haines et al. (2018) also conducted a systematic survey of X-ray groups in the infall region of 23 clusters at $z \sim 0.2$. They

estimated that the galaxy clusters typically accrete 32% of their mass by redshift zero through the accretion of these surrounding X-ray groups.

Weak gravitational lensing is another method for estimating the amount of mass in the outskirts of clusters (e.g., Geller et al. 2013; Umetsu & Diemer 2017). Unlike the X-ray mass estimates, weak lensing mass estimates are independent of the cluster dynamical state. The estimated mass in the infall region derived from weak lensing observations is consistent with caustic estimates from dense redshift surveys (Geller et al. 2013).

Combining these complementary probes strongly constrains the mass within the cluster and its infall regions. Each method of measuring the potentially infalling mass has limitations. For example, mass estimates based on the X-ray depend on the assumption of hydrostatic equilibrium. Dense spectroscopy is critical. Without redshifts, the association between extended X-ray emission and the main cluster is ambiguous. Weak lensing mass estimates may be contaminated by the presence of foreground/background systems (e.g., Hoekstra et al. 2011; Geller et al. 2013; Hwang et al. 2014). The redshift survey facilitates the separation of cluster members from these foreground/background structures.

Here we combine spectroscopy, X-ray, and weak lensing observations to study the future mass accretion by the nearby massive cluster A2029. A2029 is one of the most massive clusters at $z = 0.079$, and has been well studied with *ROSAT*, *XMM*, *Suzaku*, and *Chandra* observations (e.g., Lewis et al. 2002; Clarke et al. 2004; Walker et al. 2012; Paterno-Mahler et al. 2013). Gonzalez et al. (2018) investigated the A2029–A2033 system based on a weak lensing map using CFHT images. More recently, McCleary et al. (2018) constructed a weak lensing map of A2029

using deep DECam images. Sohn et al. (2017) conducted a redshift survey of this cluster (see also Tyler et al. 2013). They examined the statistical properties of the A2029 member galaxies, including luminosity, stellar mass, and velocity dispersion functions.

The complete redshift survey we discuss extends the survey of Sohn et al. (2017). Based on complete spectroscopy, we investigate the core of A2029 and its infall region. We identify two relatively massive subsystems in the infall region and investigate their physical properties based on spectroscopy, X-ray, and weak lensing maps. In this process, we refine the X-ray estimates of the subsystem masses. We probe the future dynamical evolution of the A2029 system based on the physical properties of the infalling groups.

We also use the complete redshift survey to make a census of foreground/background systems. Construction of this census is critical to removing ambiguous contributions to the mass within the infall region. Including A2029 and the two infalling groups, we find a total of 13 extended X-ray sources. Their physical properties are consistent with the well-known scaling relation between X-ray luminosity and velocity dispersion.

The combined analysis we discuss sets the stage for future large data sets, including these complementary probes of the mass distribution in and around clusters of galaxies. The eROSITA (Merloni et al. 2012), Prime-Focus Spectrograph (PFS) on *Subaru* (Takada et al. 2014), and Euclid (Amendola et al. 2018) will provide these observations for clusters with a wide range of masses and redshifts, thus tracing the detailed evolution of these systems.

We describe the redshift survey of A2029 in Section 2. We explain the identification of the cluster members using spectroscopic data in Section 3. In Section 4, we identify two groups within the infall region of A2029, along with foreground/background systems in the A2029 field. We summarize their aggregate properties by placing them on the well-known $L_X-\sigma_{cl}$ scaling relation. Finally, we discuss the past and future accretion history of A2029 (Section 5) based on the dynamical connection between A2029 and the massive infalling groups. Throughout this paper, we use the standard ΛCDM cosmology parameters: $H_0 = 70$ km s^{-1} Mpc^{-1}, $\Omega_m = 0.3$, and $\Omega_\Lambda = 0.7$.

2. Redshift Survey of A2029

A2029 (R.A., decl., z: 227.728729, 5.76716, 0.079) is one of the most massive clusters in the local universe (Sohn et al. 2017). It was once known as a relaxed cluster because of its smooth X-ray temperature profile (e.g., Sarazin et al. 1998). However, recent deep X-ray observations reveal an X-ray sloshing spiral pattern that indicates complex dynamical evolution (Clarke et al. 2004; Paterno-Mahler et al. 2013). Furthermore, the X-ray observations identify nearby extended X-ray sources that may be galaxy systems that will eventually accrete onto the cluster (Walker et al. 2012). To understand the dynamical status and structure of A2029, a dense redshift survey is important. Therefore, we extend the redshift survey for A2029 (Sohn et al. 2017). We include the total list of 4376 redshifts in Table 1 of this section.

2.1. Photometry

The galaxy catalog for the A2029 field is based mainly on the Sloan Digital Sky Survey (SDSS) Data Release 12 (DR12; Alam et al. 2015). Following Sohn et al. (2017), we first select extended objects with $r_{petro,0} < 22$ mag within $100'$ of the cluster center. Extended objects have $probPSF = 0$, where the $probPSF$ is the probability that the source is a star. We visually inspect extended sources and remove some suspicious objects, including stellar bleed trails and fragments of galaxies. In the northeastern part of A2029, there is a small patch with an area of ~52 arcmin^2 where the SDSS DR12 photometry is missing. We supplement the A2029 galaxy catalog with the SDSS DR7 galaxy catalog for this region. The mean r-band magnitude difference between SDSS DR7 and DR12 of the galaxies with redshifts and within $17 < r < 20.5$ is ~0.003 mag. Thus, the compilation of DR7 photometry does not introduce a systematic effect.

Following Sohn et al. (2017), we use the $ugriz$ composite model (cModel) magnitudes, a linear combination of de Vaucouleurs and model magnitudes. We apply the foreground extinction correction for each band. Throughout this paper, all magnitudes indicate extinction-corrected cModel magnitudes. Our A2029 galaxy catalog contains 96,082 extended objects brighter than $r = 22$ mag within $R_{cl} < 100'$.

2.2. The Redshift Survey

Based on the photometric galaxy catalog, we conducted a spectroscopic survey of A2029. We first collect redshifts from previous redshift surveys including SDSS DR12. The SDSS acquires spectra using $3''$ fibers for bright galaxies with $r < 17.77$. In the A2029 field within $R_{cl} < 100'$, 3109 objects have SDSS DR12 redshifts with a typical uncertainty of 7 km s^{-1}. Within $R_{cl} < 40'$, there are 731 (476) objects with SDSS DR12 (DR7) redshifts; Gonzalez et al. (2018), who investigated the A2029–A2033 system, used SDSS DR7 for the source of their redshifts.

We also compiled 1308 redshifts from Tyler et al. (2013), who carried out a redshift survey using Hectospec, mounted on the MMT 6.5 m telescope. Hectospec (Fabricant et al. 2005) is a 300 fiber-fed spectrograph that can obtain ~250 spectra with a single exposure. Tyler et al. (2013) obtained spectra of A2029 galaxies and measure the redshifts and Hα equivalent widths to study star-forming galaxy evolution in the cluster environment. The spectra taken from Tyler et al. (2013) are available through the MMT archive.[7] From these spectra, we measure the redshifts and visually inspect the redshift fits (see below for details) for consistency with the rest of our survey. Additionally, we added 440 redshifts from the literature (e.g., Bower et al. 1988; Sohn et al. 2015) through the NASA/IPAC Extragalactic Database (NED).

We conducted a deeper redshift survey of A2029 also using MMT/Hectospec. Sohn et al. (2017) reported 982 redshifts of A2029 members. Here we extend the redshift survey by including fainter objects. We use the 270 line mm^{-1} Hectospec grating. The resulting spectra have 6.2 Å spectral resolution and cover 3800–9100 Å. The typical exposure time for each field is 1 hr.

We used the IDL HSRED v2.0 package, developed by R. Cool and modified by MMT TDC, to reduce the data. We measure the redshifts based on the cross-correlation of observed spectra with a set of templates using RVSAO (Kurtz & Mink 1998). The cross-correlation results are visually inspected and classified into three groups: "Q" for high-quality fits, "?" for ambiguous cases, and "X" for poor fits. We obtained a total of 2890 high-quality redshifts with a median

---

[7] http://oirsa.cfa.harvard.edu/archive/search/

Table 1
The Redshift Catalog of A2029

SDSS Object ID	R.A.	Decl.	$r_{cModel,0}$	z	z Source[a]	Membership[b]
1237658780557836308	227.740259	5.766147	16.44	0.07731 ± 0.00010	2, 3	Y
1237658780557836317	227.750323	5.756988	17.63	0.08463 ± 0.00009	2	N
1237658780557836338	227.737793	5.762320	19.07	0.07593 ± 0.00007	2	Y
1237658780557836305	227.744635	5.770809	16.45	0.07455 ± 0.00007	2, 3	Y
1237658780557836311	227.738249	5.754465	17.90	0.07726 ± 0.00009	2	Y
1237658780557836336	227.732202	5.761856	18.47	0.08085 ± 0.00014	1	Y
1237658780557836342	227.749463	5.769346	18.83	0.07828 ± 0.00007	2	Y
1237658780557836316	227.735039	5.751555	17.46	0.07921 ± 0.00008	1, 2	Y
1237658780557836337	227.732491	5.765348	19.37	0.07899 ± 0.00006	2	Y
1237658780557836369	227.731678	5.764879	20.01	0.07735 ± 0.00015	1	Y

Notes.
[a] The sources of redshifts: (1) this survey, (2) Tyler et al. (2013), (3) SDSS, (4) NED, and (5) Sohn et al. (2015).
[b] The membership determined based on the caustics.

(This table is available in its entirety in machine-readable form.)

redshift uncertainty of 32 km s⁻¹; 1388 of these redshifts are new here compared to Sohn et al. (2017). Among these, 97 objects are stars with $|cz| < 500$ km s⁻¹ (see the Appendix).

There are 321 objects with both SDSS and MMT spectra. The redshifts from SDSS and MMT for the duplicated objects have $|\Delta cz/(1 + z_{SDSS})| \leqslant 14$ km s⁻¹. For these objects, we use the redshift from the MMT.

Figure 1 displays the completeness of the A2029 redshift survey. Figure 1(a) shows the completeness as a function of r-band magnitude. We investigate the completeness within $R_{cl} < 30'$ and $<40'$. The integrated completeness to $r_{petro,0} = 20.5$ mag within $R_{cl} < 30'$ is 90.2% (66.5% within $R_{cl} < 40'$). Figure 1(b) shows the two-dimensional completeness map for the redshift survey. The redshift survey is uniformly $\gtrsim 90\%$ complete within $R_{cl} < 30'$. The survey completeness declines rapidly outside $R_{cl} = 30'$. Nevertheless, we use the redshift survey data within $40'$ (4376 redshifts) because A2033 is included in this larger field of view. The yellow plus signs in Figure 1(b) mark the positions of galaxy systems at the A2029 redshifts: A2029, A2033, and the southern infalling group (SIG; see below).

2.3. The Redshift Catalog

Table 1 lists all of the spectroscopic redshifts within $40'$ of A2029, including redshifts from our survey and the literature. Table 1 includes the SDSS object ID, R.A., decl., r-band cModel magnitude, redshift and its error, and source of the redshift. The table also includes the A2029 membership determined based on the caustics (Diaferio & Geller 1997; see Section 3). In total, there are 4376 redshifts for galaxies in the field.

Figure 2 shows the redshift distribution of galaxies in the A2029 field. The dominant peak in the distribution at $z \sim 0.08$ is A2029. Several less dominant peaks appear at higher redshift. These peaks include several readily identifiable background groups and one foreground group (see Section 4.2).

Figure 3 displays the cone diagram for galaxies in the A2029 field projected along the R.A. direction. Black points are the galaxies brighter than $r_{cModel,0} = 20.5$, and gray points are fainter galaxies. A2029 is the densest feature in the field. In the background of A2029, the cone diagram shows the characteristic large-scale structure characterized by sizable voids and
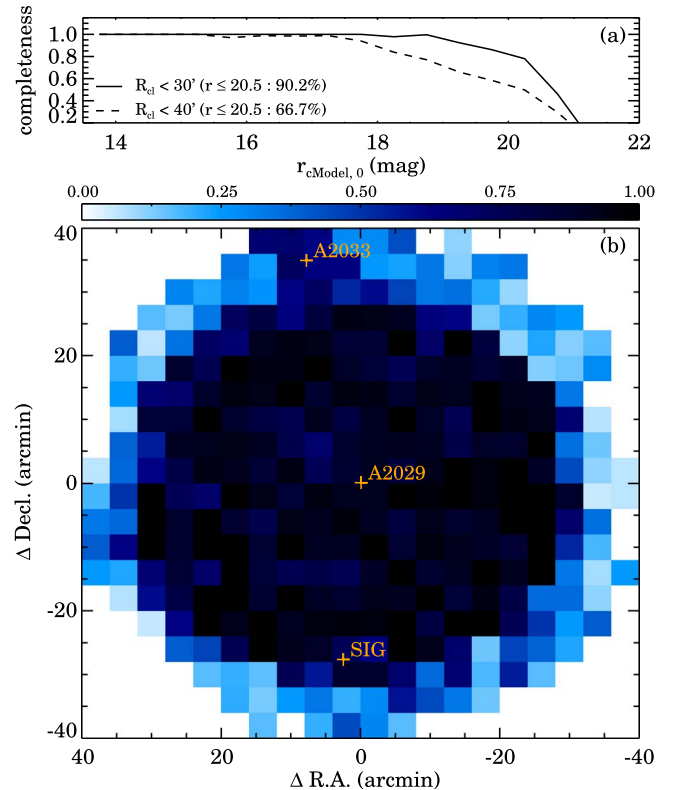

Figure 1. (a) Spectroscopic survey completeness as a function of r-band magnitude. The solid and dashed lines plot the completeness within $R_{cl} < 30'$ and $<40'$, respectively. The survey is $\sim 90\%$ complete to $r_{petro,0} = 20.5$ mag within $R_{cl} < 30'$. (b) Two-dimensional map of the redshift survey completeness to $r_{petro,0} = 20.5$ mag within $R_{cl} < 40'$. The yellow plus signs mark the centers of A2033, A2029, and the SIG (from top to bottom).

thin dense structures. Even corrected for the magnitude selection, all of these background structures are much less dense than A2029.

3. Member Selection

The caustic technique (Diaferio & Geller 1997; Diaferio 1999; Serra & Diaferio 2013) is a powerful tool for identifying cluster members based on a spectroscopic survey. The caustic
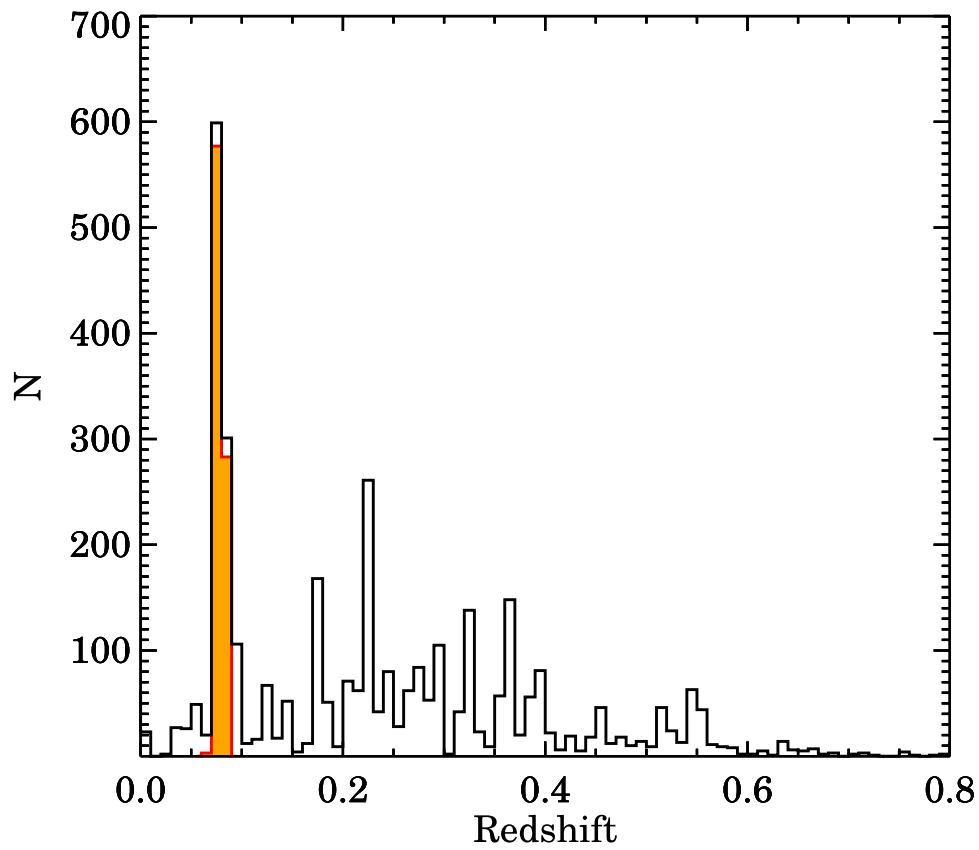
Figure 2. Redshift distribution of galaxies in the A2029 redshift survey. The filled histogram shows A2029 members identified based on the caustics.
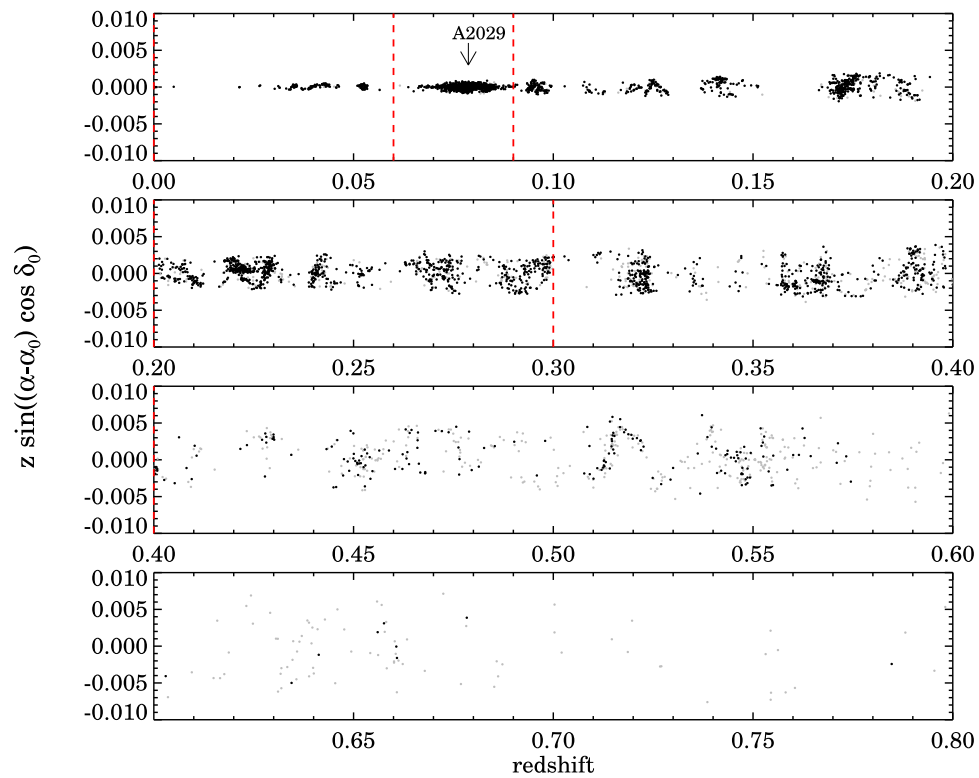

Figure 3. Cone diagram of the A2029 field within $R_{cl} < 40'$ projected in the R.A. direction. Black (gray) points are the galaxies brighter (fainter) than $r_{cModel,0} = 20.5$. Dashed vertical lines display the boundaries we use for identifying galaxy surface number densities that correspond to groups as described in Section 4.2.
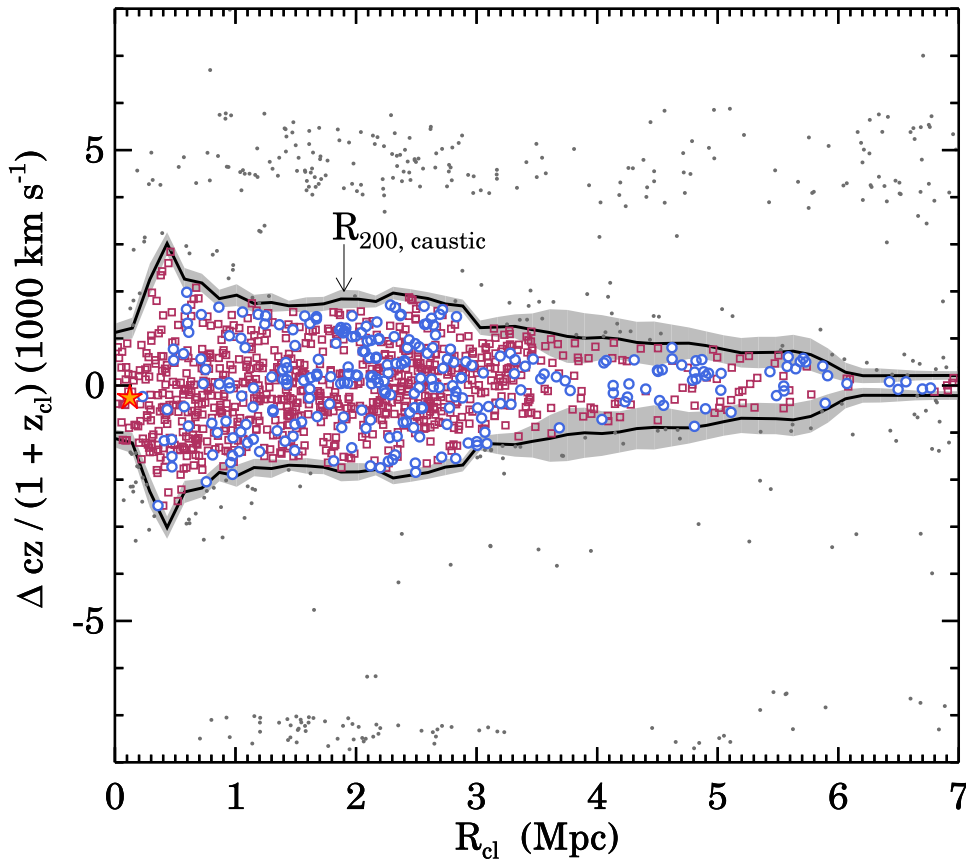
Figure 4. The R–v diagram for A2029. Gray dots are individual galaxies with redshifts. Red squares and blue circles are quiescent ($D_n 4000 > 1.5$) and star-forming ($D_n 4000 \leqslant 1.5$) members of A2029, respectively. The star shows the BCG of A2029 (IC 1101). The rest-frame line-of-sight velocity difference between the BCG and the cluster means is -170 ± 107 km s^{-1}. The arrow indicates R_{200} derived from the caustic mass profile.

technique calculates the escape velocity from the cluster and provides a mass profile of the cluster as a function of projected distance from the cluster center. As a by-product, the technique identifies cluster members within the caustic pattern. Serra & Diaferio (2013) showed that the technique successfully identifies ~95% of cluster members within $3R_{200}$ from mock catalogs with ~1000 galaxies including ~180 members per cluster. The contamination from the interlopers is small: ~2% within R_{200} and ~8% within $3R_{200}$.

Figure 4 shows the relative rest-frame line-of-sight velocity difference versus the projected distance for A2029, the R–v diagram. In this phase space, a typical cluster shows a well-defined trumpet-like pattern (Kaiser 1987; Regos & Geller 1989). The solid lines show the caustics we derive based on the A2029 spectroscopic data, and the shaded regions display the uncertainty in the caustic location. The caustics distinguish clearly between the cluster members and other galaxies along the line of sight. Gaps between cluster members and the foreground/background galaxies are intrinsic to the large-scale galaxy distribution; they do not originate from the incompleteness of the redshift survey.

We derive the characteristic mass M_{200} and radius R_{200} based on the caustics: $M_{200} = 8.47^{+0.25}_{-0.23} \times 10^{14}$ $M_\odot$ and $R_{200} = 1.91^{+0.17}_{-0.19}$ Mpc. Here M_{200} and R_{200} indicate the mass and radius where the mean density is 200 times the critical density of the universe. The derived M_{200} and R_{200} are consistent with the values we derived in Sohn et al. (2017) based on a somewhat less complete redshift survey. The spectroscopically derived M_{200} and

R_{200} are also compatible with those based on the X-ray temperature profile (Walker et al. 2012): the $M_{200,\text{X-temp}}$ is $8.0^{+0.15}_{-0.15} \times 10^{14}$ $M_\odot$, and the $R_{200,\text{X-temp}}$ is $1.92^{+0.11}_{-0.13}$ Mpc. We also calculate the velocity dispersion of A2029 following the recipe given in Danese et al. (1980). We use the 571 members within $R_{\text{cl}} < R_{200}$. The velocity dispersion of A2029 is 967 ± 25 km s^{-1}, consistent with the value derived in Sohn et al. (2017).

We identify 1215 spectroscopic members of A2029 within the caustics; 571 cluster members are within R_{200}. The number of A2029 members exceeds that of Sohn et al. (2017), who reported 982 spectroscopic members. A2029 is one of the best-sampled clusters. There are 441 members in A2029 with $M_r < -18$ and $R_{\text{cl}} < R_{200}$; Coma has 530 members with the same selection (Sohn et al. 2017). Hereafter, we refer to the 1215 spectroscopic members within the caustics as members of the A2029 system and the 571 members within $R_{\text{cl}} < R_{200}$ as members of A2029.

A2029 contains the most massive Brightest Cluster Galaxy (BCG; IC 1101) in the local universe (Uson et al. 1991). We investigate the projected distance between the BCG and the X-ray center following previous studies. Patel et al. (2006) reported that the BCG of A2029 is 131 kpc from the X-ray peak. However, they used the X-ray center based on *ROSAT* data with a large point-spread function (PSF). Lauer et al. (2014) demonstrated that there are significant differences between the *ROSAT* and *Chandra* X-ray centers for a significant fraction of their cluster sample. Indeed, the offset between the A2029 BCG

and the *Chandra* X-ray position is only 0.42 kpc (see 1 kpc in Lauer et al. 2014).

Next, we examine the position of the A2029 BCG with respect to the cluster center in redshift space (Figure 4). The projected offset (ΔR_{cl}) is 123 ± 170 kpc, and the radial velocity offset in the rest frame of the cluster is -170 ± 107 km s^{-1}. The positional uncertainties include the error in the caustic center (Serra et al. 2011). Within the uncertainty, IC 1101 lies in the kinematic center of A2029.

4. Structure of the Massively Accreting Cluster A2029

Current structure formation models suggest that galaxy clusters grow hierarchically through the accretion of lower-mass systems (e.g., Bond et al. 1996; Colberg et al. 2005). Mass estimates for infalling groups provide a direct estimate of the mass accretion rate (or the growth rate; De Boni et al. 2016; Haines et al. 2018).

Systems around clusters can be identified independently with X-ray, lensing, photometric, and spectroscopic observations. Systematic X-ray surveys show that many local clusters have X-ray-emitting groups in the infall regions (Rines et al. 2002; Haines et al. 2018). These X-ray-emitting groups may be accreting systems (e.g., Rines et al. 2002; Haines et al. 2018). Gravitational lensing is another sensitive tool for identifying accreting groups by tracing the mass distributions in the cluster field (Okabe et al. 2010; Martinet et al. 2016). A dense spectroscopic survey enables the detection of lower-mass systems around the cluster (Yu et al. 2015, 2016, 2018; Liu et al. 2018). This method has the advantage that the redshifts of the lower-mass systems are known; the X-ray and lensing candidate systems may not be at the main cluster redshift.

Here we search for galaxy groups around A2029 based on all of these methods (Section 4.1). Taking advantage of the redshift survey, we construct a number density map of cluster members that facilitates group identification. We also utilize both the weak lensing map and X-ray observations of the cluster to obtain the physical properties of the groups. We describe the identification of foreground/background groups in Section 4.2.

4.1. Infalling Groups

Figure 5(a) is a schematic view of the A2029 field. A2029 is at the center of the field. Red plus signs mark the positions of possibly infalling groups associated with A2029. These groups correspond to peaks in the number density map of spectroscopic members. A2033 is one of these groups; we display the A2033 center from NED. We also display the center of the SIG. Several additional galaxy overdensities appear in the surface number density map of the spectroscopic survey; black crosses/plus signs show galaxy overdensities with/ without X-ray counterparts (see Section 4.2). The solid circle centered on A2029 is the R_{200} based on the caustics. The dashed circles are the R_{200} of A2029, A2033, and SIG, measured based on their X-ray luminosities (Section 5.1).

Figure 5(b) shows a surface number density map for the spectroscopically identified members of A2029. For comparison, we plot a background color map displaying the number density of photometric galaxies with $r \leqslant 20.5$ in the A2029 field. To avoid confusion, we refer to the surface number density maps of members and of photometric galaxies as the member density map (contour) and the galaxy density map (color map), respectively.

The member density map of A2029 is complex. Overall, the distribution is elongated in the north–south direction. At the northern edge, a complicated structure includes A2033. The member density peak of A2033 is slightly offset from the peak in the photometric galaxy density map. The offset results from contamination by background galaxies (see Section 4.2). The southern group matches the peak of the photometric galaxy density map. A2033 is seven times and SIG is four times more dense than the mean number density of spectroscopic members within a 500 kpc width annulus at a similar clustercentric distance.

Figure 5(c) shows a weak lensing map of the A2029 field. McCleary et al. (2018) used DECam imaging covering a 2.5 deg^2 field to construct the weak lensing map from $\sim$160,000 galaxies with shapes ($\sim$17 galaxies arcmin^{-2}) and five-band photometric redshift estimates. The full description of the weak lensing analysis is contained in McCleary et al. (2018) here we provide only a brief summary.

The A2029 field was observed in the *ugriz* filters in three runs between 2013 and 2015, with total exposure times ranging from 12,200 s in *u* to 3150 s in *r*. The shapes for weak lensing were derived from the *i* imaging, where the mean seeing was 0″9. The DECam data were processed using the NOAO community pipeline,[8] and then stacks and PSF modeling were done using the THELI pipeline (Erben et al. 2001). Galaxy shapes were computed using the KSB algorithm, as implemented in Erben et al. (2001) and von der Linden et al. (2014). Galaxy photometry was calibrated by comparing photometric catalogs to the SDSS catalog of the sky, and all galaxies with a half-light radius greater than 1.15 and model PSF size brighter than the 50% completeness limit ($i = 24.4$ for A2029) are used in the weak lensing analysis (a total of 160,256 galaxies). Photometric redshifts based on the galaxy colors are assigned using BPZ (Benítez 2000), and galaxies to which BPZ assigns a probability that $z > 0.18$ (0.1 greater than the redshift of A2029) greater than 85% are used in the mapping.

Gonzalez et al. (2018) also presented a weak lensing analysis of A2029 based on CFHT images. However, the lensing map of Gonzalez et al. (2018) covers only A2029 and A2033. Gonzalez et al. (2018) used the catalog and CFHT MegaCam images with better ($\sim$0″6) seeing but exposure times of only 500 s and only two filters (*ri*), and Gonzalez et al. (2018) used all objects with a >70% chance of being a background object based on two-band colors. Furthermore, the typical number density of galaxies in their analysis is 3.5 galaxies arcmin^{-2}, a factor of five lower than McCleary & Dell'Antonio's source density. Thus, the significance of the weak lensing detections is higher in McCleary & Dell'Antonio's map, enabling detection of SIG and providing smaller errors in the A2029 and A2033 mass estimates.

To map out the projected mass distribution, we use the aperture mass statistic (Schneider 1996) with a compensated filter (Schirmer et al. 2004), which provides an effective smoothing scale of 2′5 for the map. The significance of the signal at each pixel in the map is estimated by constructing 2×10^6 randomized realizations in which the shapes of the galaxies are randomly shuffled and then measuring how often the randomized signal exceeds the true signal (see McCleary et al. 2015). These significance measures are converted to an equivalent σ confidence for display in Figure 5(c).
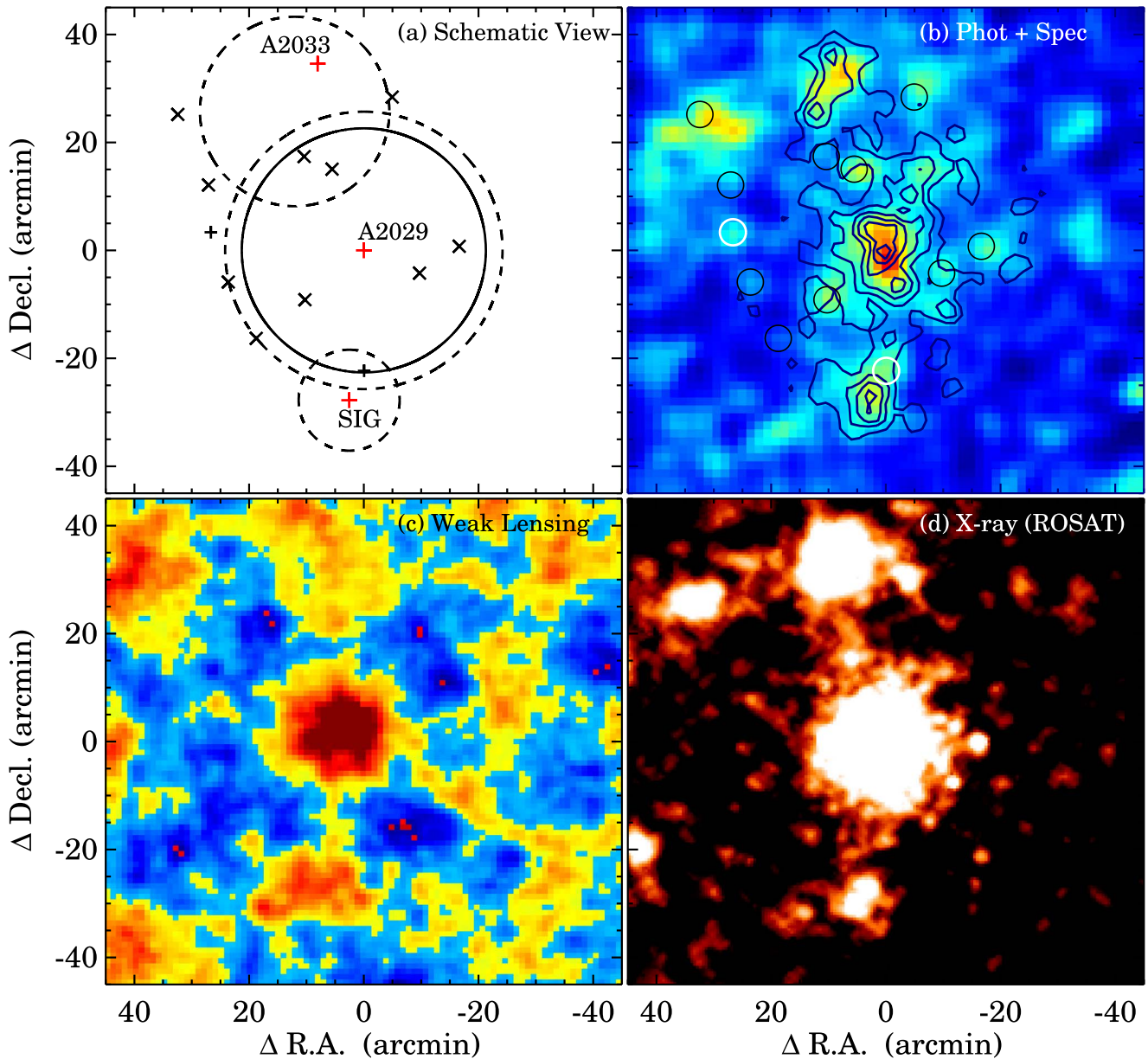
---

[8] NOAO Data Handbook v2.2.

Figure 5. Multiwavelength view of A2029. (a) Schematic view of the A2029 field. Red plus signs mark the positions of A2029, SIG, and the previously known center of A2033. Black crosses and plus signs are the position of overdensities shown in the surface number density map of the galaxy distribution. Crosses have X-ray counterparts; plus signs do not. The solid circle indicates R_{200} derived from the caustic mass profile, and the dashed circles are R_{200} estimated from the L_X-M_{200} relation from Leauthaud et al. (2010). (b) Galaxy distribution in the A2029 field (colored map) compared with the number density map of spectroscopically identified A2029 members (contours). (c) Weak lensing significance map of A2029 based on DECam imaging (McCleary et al. 2018). Red indicates high significance, and blue indicates low significance. (d) *ROSAT* X-ray map of the A2029 region.

The detection significance for a subclump is taken to be the highest-significance pixel. For A2029, the signal is so strong that none of the randomized realizations showed as strong a lensing signal, indicating a detection at >5σ. For both A2033 and SIG, the situation is complicated by the complex morphology in the lensing map, where multiple pixels have similar significance. We choose to follow the "highest-pixel" prescription and report a significance of 3.0σ for A2033 and 3.3σ for SIG.

The morphology of the weak lensing map is similar to that of the photometric galaxy density map. The strongest peak is the core of A2029. A2033 and SIG are also detected with high significance. Other overdensities in the surface density map also correspond to low-significance features in the lensing map.

The consistency between the lensing map and the photometric galaxy density map is expected because the lensing map traces the cumulative projected mass density along the line of sight and within the weak lensing kernel. Okabe et al. (2010) showed maps for other systems with similar qualitative correspondence.

Figure 5(d) displays the *ROSAT* X-ray image of the A2029 field. We use the image from the *ROSAT* Position Sensitive Proportional Counter (PSPC) observation (program ID: rp800249; PI: C. Jones). The *ROSAT* PSPC data were reduced using the *ROSAT* Extended Source Analysis Software (ESAS; Snowden et al. 1994). The image is background-subtracted and exposure-corrected in the R47 band (0.44–2.04 keV, as shown in Walker et al. 2012).

Table 2
The Positions of A2029, A2033, and SIG

ID	R.A.	Decl.	Redshift	BCG R.A.	BCG Decl.	BCG Redshift
A2029	227.728729	+5.767164	0.0787	227.733751	+5.744775	0.0778
A2033	227.863556	+6.340870	0.0812	227.860464	+6.349078	0.0810
SIG	227.771622	+5.304444	0.0802	227.780800	+5.317282	0.0783

Bright X-ray emission is present at the centers of A2029 and A2033. These X-ray sources are listed in the *ROSAT* Brightest Cluster Sample (Ebeling et al. 1998). There is also clear X-ray emission near the SIG (the second *ROSAT* PSPC catalog; Rosat 2000). Walker et al. (2012) mentioned the existence of this southern extended X-ray source.

The spectroscopy, weak lensing, and X-ray images paint a consistent view of the structure associated with A2029 within $R_{cl} < 40'$. The core of A2029 is a massive galaxy system associated with bright extended X-ray emission. Two groups, A2033 and SIG, appear in all three maps. Table 2 summarizes the positions of A2029 and these groups.

A2033 was known as a separate cluster from A2029 (Abell et al. 1989). Several cluster-finding algorithms based on the SDSS photometric galaxy catalog also identify this cluster (Wen et al. 2009, 2012; Hao et al. 2010; Szabo et al. 2011). A2033 is also listed in the *ROSAT* X-ray Brightest Cluster Sample (Ebeling et al. 1998). Based on redshifts from NED and SDSS spectroscopy, Sifón et al. (2015) identified ~190 spectroscopic members of A2033 at a mean redshift of $z_{A2033} = 0.0796$. They computed R_{200} (=1.89 ± 0.14 Mpc) and σ_{200} (=911 ± 69 km s⁻¹) based on these members.

Figure 6(a) shows an R–v diagram centered on A2033. Within the R_{200} from Sifón et al. (2015) and $|\Delta cz/(1 + z_{A2033})| < 2000$ km s⁻¹, there are 223 member galaxies. As expected from the member density map, most A2033 members are within the A2029 caustics, except for a few outliers with large velocities relative to the mean or A2029. The member distributions of A2029 and A2033 overlap in the phase-space diagram, making the identification of most members associated with A2033 ambiguous. The location of A2033 within the caustics suggests that it is dynamically connected to A2029 (see Rines et al. 2002).

Figure 6(b) displays the spatial distribution of the galaxies in the A2033 field. The background map shows the two-dimensional redshift survey completeness to $r_{cModel,0} = 20.5$. The open and filled circles are the spectroscopic targets and A2033 members, respectively. The A2033 members have an elongated distribution (contours); they are offset from both the brightest group galaxy (BGG) of A2033 (star symbol) and the *Chandra* X-ray center (cross). Because the redshift survey is homogeneous around the center of A2033, the elongated distribution of the cluster members is not a product of incompleteness in the survey. Southeast of A2033, there is a loose concentration of galaxies at $z \sim 0.27$. Thus, the over-density in the galaxy density map shown in Figure 5(b) is contaminated by background galaxies. We conclude that the offset between the peak of the A2033 galaxy distribution and the A2033 BGG (or the X-ray center) is a physical property of the system. The mean redshift of the A2033 members is $z_{A2033} = 0.0812$, slightly larger than the mean redshift from Sifón et al. (2015).

The BGG of A2033 is only ~5 kpc from the *Chandra* X-ray center. The large offset (179 kpc) listed in Patel et al. (2006) is
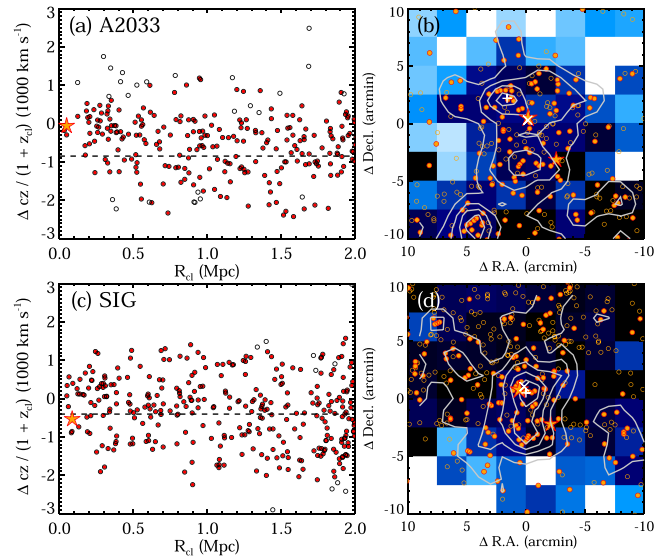

Figure 6. (a) R–v diagram centered on A2033. Open circles are the spectroscopic targets, and filled circles are the A2029 members within the caustics. The star symbol indicates the brightest galaxy of A2033. The horizontal dashed line indicates the mean redshift of A2029. (b) Galaxy distribution in the A2033 field. The background map is the two-dimensional redshift completeness map. Open and filled circles are the spectroscopic targets and A2033 members, respectively. The star symbol is the A2033 BGG. The gray contours are the number density map of the A2033 members. The cross is the X-ray peak from the *Chandra* observations (ObsID: 15167; PI: T.Reiprich) The plus symbol is the peak of the surface number density map of the A2033 members. (c) and (d) Same as (a) and (b) but for SIG. The cross in panel (d) is the X-ray peak determined based on the *ROSAT* data.

an overestimate due to the large uncertainty in the *ROSAT* X-ray center. In contrast to the X-ray, the BGG of A2033 is certainly offset (~250 kpc) from the peak surface number density of A2033 members (panel (b) of Figure 6). The astrophysical implications of this offset are unclear. The radial velocity difference between the BGG and A2033 mean is not significant (~−57 km s⁻¹).

We show the R–v diagram and the spatial distribution of the galaxies in the SIG field in Figures 6(c) and (d). There is no clear separation between the SIG members and the A2029 members. The brightest galaxy in SIG is significantly offset from the kinematic center of SIG. Furthermore, the spatial distribution of the SIG members is also elongated in the N–S direction, as is A2033. The mean redshift of SIG is $z_{A2033} = 0.0802$.

Measuring the offset between the BGG of SIG and the X-ray peak is challenging because the *ROSAT* X-ray morphology of SIG is disturbed. The northern peak in the *ROSAT* image corresponds to the BGG of SIG. The BGG offset from the northern X-ray peak is 38 kpc. The BGG is coincident with the surface number density peak of the SIG members ($\Delta R_{cl} = \sim45$ kpc; panel (d) of Figure 6). Interestingly, the BGG is ~-533 km s⁻¹ from the mean for SIG, a much larger difference than for the brightest galaxies of A2029 and A2033.

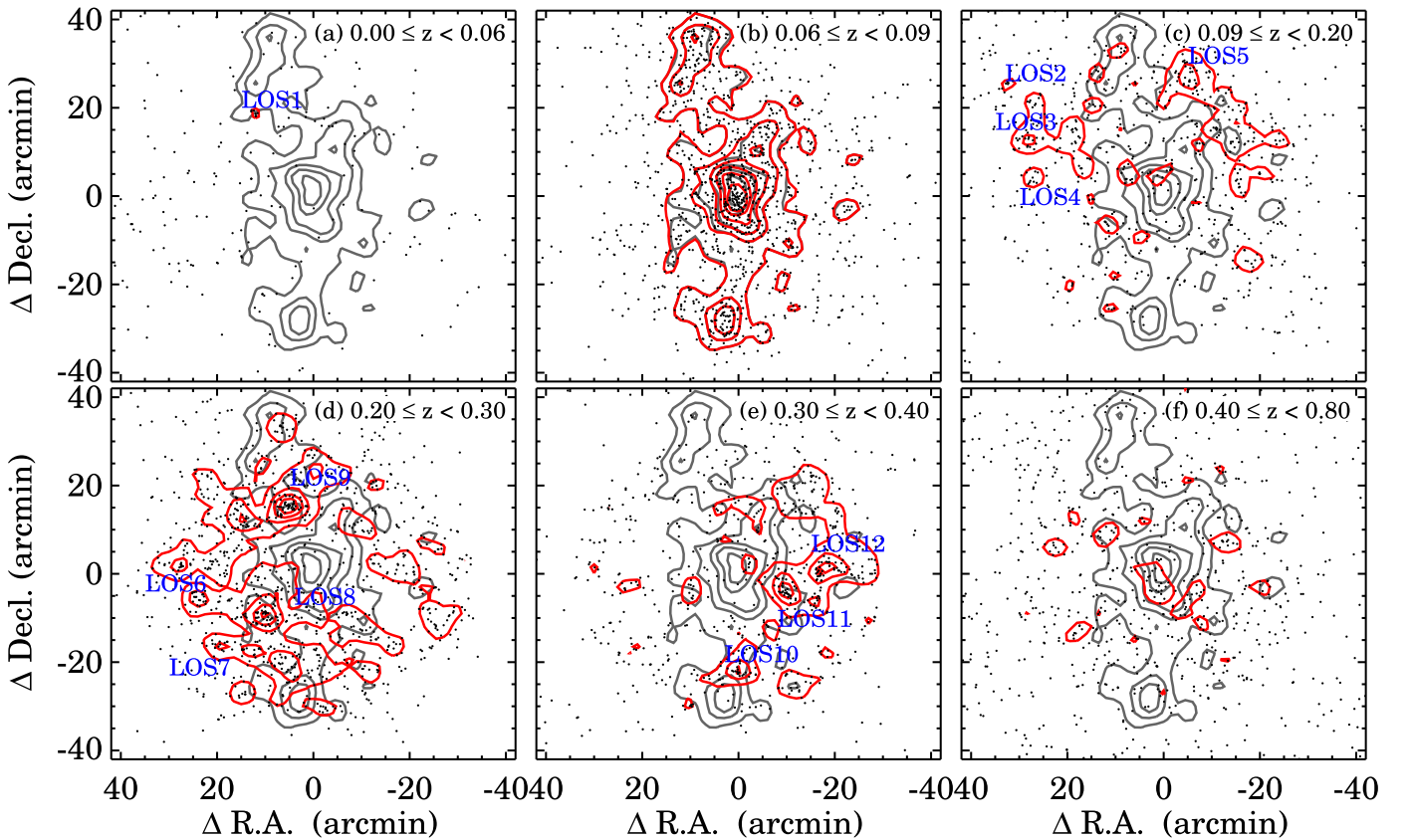**Figure 7.** Red contours show surface density maps for galaxies in different redshift ranges: (a) $0 \leqslant z < 0.06$, (b) $0.06 \leqslant z < 0.09$ (mainly A2029), (c) $0.09 \leqslant z < 0.20$, (d) $0.20 \leqslant z < 0.30$, (e) $0.30 \leqslant z < 0.40$, and (f) $0.40 \leqslant z < 0.80$. Black points are individual galaxies. The gray contours show the surface number density map for spectroscopic members of A2029. The lowest surface number density contour is 0.28 galaxies arcmin^{-2}; the contours increase in steps of 0.28 galaxies arcmin^{-2}.

We identify the two subsystems, A2033 and SIG, associated with A2029 based on spectroscopy, weak lensing, and X-ray maps. A2033 and SIG appear in all three probes. We discuss the physical properties and implications of these subsystems for the future evolution of the A2029 system in Section 5.3. We also identify additional foreground/background groups unassociated with A2029 and evaluate their properties in Section 4.2.

4.2. Foreground/Background Groups in the A2029 Field

The multiwavelength maps reveal several foreground/background groups in the A2029 field. The cone diagram (Figure 3), the galaxy surface density map, the weak lensing significance map, and the X-ray images in Figure 5 all show some concentrations of galaxies unassociated with the cluster. Consideration of all of these systems that may artificially contribute to the number density, X-ray, and weak lensing map requires a dense, deep spectroscopic survey and is thus not treated by Gonzalez et al. (2018).

We examine the surface number density maps for galaxies in different redshift slices to identify foreground/background groups. The dashed vertical lines in Figure 3 indicate the boundaries of the six subsamples we consider. Each subsample includes a few probable groups.

Figure 7 displays surface density maps for each of the redshift subsamples. Black points indicate individual galaxies in each subsample, and red contours show the corresponding surface number density map. For comparison, we show the

surface number density map for spectroscopically identified cluster members (gray contours). The lowest level of the contours is 0.28 galaxies arcmin^{-2}, and the contours increase in steps of 0.28 galaxies arcmin^{-2}.

Figure 7(a) shows the spatial distribution of objects with $0 \leqslant z < 0.06$. There are 157 galaxies in the foreground of the cluster. A small, tight group (LOS1; red contour) of 14 galaxies is at $z = 0.052$. The spectroscopic members are within the simple window: $R_{cl} < 500$ kpc and $|\Delta cz/(1 + z_{cl})| \leqslant 2000$ km s^{-1}. We display the R–v diagram of this system in Figure 8(a). The velocity dispersion of the system is $\sigma = 252 \pm 11$ km s^{-1}.

We plot the galaxies with $0.06 \leqslant z < 0.09$ in Figure 7(b). The galaxies in this redshift range are mostly cluster galaxies. The surface number density map of the galaxies is essentially identical to the cluster member density map. The contribution of noncluster members to the surface number density of the cluster member is negligible.

Figure 7(c) is based on 676 galaxies with $0.09 \leqslant z < 0.20$. We identify four groups (LOS2–LOS5) with more than nine members. These groups correspond to peaks in the photometric galaxy density map in Figure 5(b), but they are unrelated to A2029. The R–v diagrams of the groups are in panels (b)–(e) of Figure 8.

Figure 7(d) shows the distribution of 1052 galaxies in the range $0.20 \leqslant z < 0.30$. We identify at least four groups (LOS6–LOS9). Each group contains a significant number ($N > 12$) of members except LOS7, which is a superposition of galaxies at different redshifts. The other LOSs match the
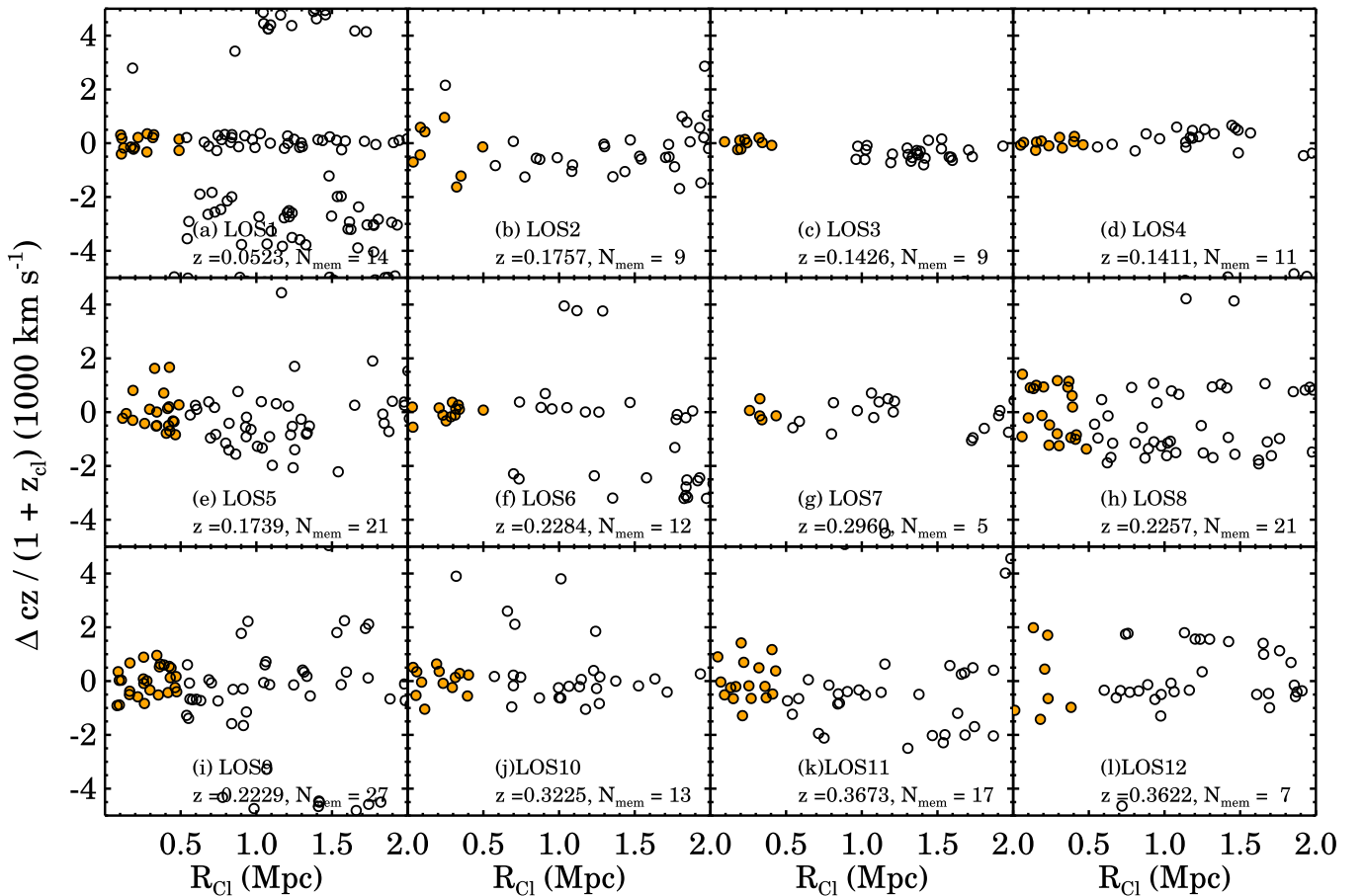
Figure 8. The R–v diagrams of the foreground/background groups in the A2029 field. The open circles are spectroscopic targets. The orange filled circles are the members of the groups within $R_{cl} < 5'$ and $|\Delta cz/(1 + z_{cl})| < 2000$ km s^{-1}.

galaxy overdensities in the photometric galaxy density map (Figure 5(b)).

LOS8 at $z = 0.226$ is a complicated structure including 21 spectroscopic members (Figure 8(h)). The redshift distribution of LOS8 members is bimodal. However, the spatial distributions of the galaxies in the two redshift groups are indistinguishable. LOS8 may be a group undergoing a merger.

LOS9 with 25 members has associated X-ray emission. Figure 8(i) plots the R–v diagram for this group. Walker et al. (2012) found X-ray emission near LOS9 based on *ROSAT* imaging data. They suggested that the X-ray source originates from the overlap of X-ray emission from A2029 and A2033. However, the surface number density map indicates that the X-ray emission is actually from a background system that appears as a finger in the cone diagram at $z \sim 0.223$. The X-ray flux of this system from the *ROSAT* PSPC data is 6.17×10^{-13} erg s^{-1} cm^{-2}, corresponding to an X-ray luminosity of $\sim 1.78 \times 10^{43}$ erg s^{-1}. The velocity dispersion of the system is 445 ± 18 km s^{-1}. The X-ray luminosity and velocity dispersion of LOS9 are consistent with the L_X–σ_{cl} relation derived from clusters at similar redshift (Rines et al. 2013).

Our redshift survey includes 688 galaxies with $0.30 \leqslant z < 0.40$. The projected spatial distribution of these galaxies is shown in Figure 7(e). We identify three groups within this subsample. LOS10 at $z = 0.326$ lies between A2029 and SIG. This group may impact the mass estimate of A2029 based on weak lensing. LOS11 with 17 members is located east of the

cluster. LOS12 is a superposition of galaxies containing a group of six galaxies at $z = 0.362$.

We plot the location of the 596 galaxies in the wide redshift range $0.40 \leqslant z < 0.80$ in Figure 7(f). The redshift survey appears sparse because it includes only the most intrinsically luminous galaxies at this redshift. Thus, we cannot identify background groups in this range.

Table 3 summarizes the foreground/background groups we identify in the A2029 field. Table 3 includes the central position, redshift, number of spectroscopic members, rest-frame line-of-sight velocity dispersion, and X-ray luminosities. Here the X-ray luminosities are measured within the energy band 0.1–2.4 keV based on the *ROSAT* image. The identification of these structures in the cluster field enables further understanding of the multiwavelength view of the cluster. For example, the apparent X-ray emission between A2029 and A2033 is most probably flux from a background system at redshift $z = 0.223$.

5. The Past and Future of A2029

The dynamical history of A2029 is complex. Deep *Chandra* X-ray observations reveal an astonishing sloshing pattern extending to 400 kpc around the BCG (Clarke et al. 2004; Paterno-Mahler et al. 2013). Hydrodynamic simulations show that the sloshing pattern can form through the interaction between the cluster and an infalling subcluster (ZuHone et al. 2010). By comparing the observed sloshing pattern with

Table 3
Structures in the A2029 Field

ID	R.A. (deg)	Decl. (deg)	Redshift	$N_{\rm mem}$[a]	σ (km s^{-1})	L_X (10^{43} erg s^{-1})
LOS1	227.902850	6.057051	0.052	14	252 ± 11	0.0453 ± 0.0041
LOS2	228.271960	6.186980	0.176	9	993 ± 41	13.1195 ± 0.3400
LOS3	228.182250	5.968993	0.143	9	130 ± 6	<0.0111
LOS4	228.175492	5.823115	0.141	11	133 ± 7	<0.0125
LOS5	227.645900	6.240714	0.174	21	597 ± 16	3.3707 ± 0.1606
LOS6	228.124521	5.669391	0.228	12	212 ± 10	<0.1072
LOS7	228.042953	5.495509	0.296	5	230 ± 9	<0.0146
LOS8	227.900588	5.614726	0.226	21	789 ± 25	3.8967 ± 0.2075
LOS9	227.821348	6.018032	0.223	27	445 ± 18	3.1008 ± 0.2119
LOS10	227.727834	5.395346	0.326	13	364 ± 12	0.8018 ± 0.0773
LOS11	227.565872	5.696886	0.367	17	535 ± 19	7.0670 ± 0.6234
LOS12	227.449909	5.779819	0.362	7	1021 ± 35	17.2136 ± 0.8321

Note.
[a] Number of spectroscopic members within $R_{\rm cl} < 500$ kpc and $|\Delta cz/(1 + z_{\rm cl})| \leqslant 1000$ km s^{-1} from the center of the structures.

hydrodynamic simulations, Paterno-Mahler et al. (2013) suggested that A2029 interacted with an infalling group with 20% of the mass of A2029 ($\sim 1.7 \times 10^{14}\ M_\odot$) between 2 and 3 Gyr ago.

Based on the maps in Figure 5, we identify two galaxy groups at the same redshift as A2029. The members of these groups are within the caustic profile of A2029, indicating that they will produce additional accretion events over the long-term future of the system. We include the complete A2029 system, in contrast with Gonzalez et al. (2018), who only treated A2029 and A2033.

Haines et al. (2018) identified similar infalling X-ray groups within the caustics of the primary clusters in the LoCuSS cluster sample. Rines et al. (2002) also identified several X-ray groups within the caustics of A2199. They computed the turnaround radius of A2199 ($\sim 6.4-8.1$ Mpc) and identified three X-ray groups within the turnaround radius and the caustic as infalling groups. The two galaxy groups of A2029 that we identify are well within the turnaround radius of A2029 (~ 10 Mpc, larger than that for A2199 because of its larger mass).

In Section 5.1, we discuss the properties of A2033 and SIG. In Section 5.2, we consider their probable future accretion by A2029. Section 5.3 discusses the accretion in a broader context, including comparison of the group masses with the total amount of material in the infall region.

5.1. The Physical Properties of the Infalling Groups

We estimate the physical properties of the infalling groups, including their membership, size, and mass. We determine the membership based on spectroscopy. Because of the proximity of the infalling groups to the cluster core, we cannot compute caustics for the groups free of contamination by members of the primary cluster. Thus, we identify group members by applying simple cuts: $R_{\rm proj} < 500$ kpc and $|\Delta cz/(1 + z_{\rm cl})| < 2000$ km s^{-1}. The projected radius cut is small enough not to overlap the R_{200} of the primary cluster. The line-of-sight relative-velocity criterion is comparable with the amplitude of the A2029 caustic at the group position. There are 57 and 70 spectroscopically identified members in A2033 and SIG, respectively. The typical numbers of projected A2029 members around the A2033 and SIG distances are 8 and 18, respectively.

The velocity dispersions of A2033 and SIG are 701 ± 74 and 745 ± 62 km s^{-1}, respectively. To evaluate the velocity dispersion and its error for A2023 and SIG, we use 1000 randomly selected subsets of 49 A2033 members and 52 SIG members. This process accounts for the average contamination by A2029 in the annulus. The velocity dispersion error indicates the 1σ deviation from 1000 velocity dispersion estimates. We derive the $M_{200,\sigma}$s and $R_{200,\sigma}$s of the groups based on the $M_{200}-\sigma$ scaling relation from Rines et al. (2013):

$$M_{200,\sigma}[10^{14}M_\odot] = 0.093$$
$$\times (\sigma/[200\ {\rm km\ s}^{-1}])^{(2.90 \pm 0.15)}. \quad (1)$$

The estimated mass is $(3.50 \pm 2.21) \times 10^{14}\ M_\odot$ for A2033 and $(4.32 \pm 2.38) \times 10^{14}\ M_\odot$ for SIG. We list the estimated $M_{200,\sigma}$ and $R_{200,\sigma}$ in Table 4.

Next, we measure the masses of the systems based on the weak lensing profile. The weak lensing mass estimates follow the procedure developed in McCleary et al. (2018) to simultaneously fit multiple mass components, taking advantage of the linearity of the lensing deflections (as opposed to the shears). Each component is modeled as an NFW profile centered on the coordinate defined by the X-ray peak. Weak lensing fits to NFW profiles are strongly degenerate in the NFW parameters; because the vast majority of the background galaxies are at $r \gg r_s$, what is constrained is not the shape of the lensing profile but the enclosed mass. In McCleary et al. (2018) rather than impose a mass-concentration relation on clusters of unknown mass, they fixed the concentration at 4 for all studies. This process makes a negligible contribution to the mass error budget, which is dominated by the random ellipticities of the background galaxies and the uncertainties in the critical density due to photo-z uncertainties. For each component, the value of the gravitational lensing deflection as a function of the component M_{200} is then derived at the position of each background galaxy using the photometric redshift of the galaxy and the cluster to define the distance ratios. We numerically compute the gradient of the deflection to calculate the predicted shear at the position of each galaxy, then vary the masses of the components to minimize the rms difference between the observed galaxy ellipticity tensors and the predicted shears. We estimate the uncertainty in the mass

Table 4
The Physical Properties of A2029, A2033, and SIG

ID	N_{mem} [a]	σ_{cl} (km s^{-1})	$M_{200,\sigma}$ [b] ($10^{14}M_\odot$)	M_{WL} ($10^{14}M_\odot$)	kT (keV)	$M_{200,\text{X-temp}}$ [c] ($10^{14}M_\odot$)	L_X (10^{43} erg s^{-1})	$M_{200,\text{X-lum}}$ [d] ($10^{14}M_\odot$)	$M_{200,\text{mean}}$ [e] ($10^{14}M_\odot$)
A2029	597	967 ± 25	9.0 ± 3.4	9.6 ± 1.8	7.5	10.87 ± 0.93	94.85 ± 0.47	17.53 ± 0.06	9.8 ± 1.3
A2033	57	701 ± 74	3.5 ± 2.3	2.4 ± 1.6	3.7	3.58 ± 0.11	17.69 ± 0.19	5.79 ± 0.04	3.2 ± 0.9
SIG	70	745 ± 62	4.2 ± 2.3	1.3 ± 1.5	...	...	0.22 ± 0.02	1.17 ± 0.02	2.8 ± 1.4

Notes.
[a] The number of spectroscopic members within R_{200} for A2029 and within 500 kpc for A2033 and SIG.
[b] $M_{200,\sigma}$ estimated based on the $M_{200}-\sigma$ relation in Rines et al. (2013).
[c] $M_{200,\text{X-temp}}$ estimated based on the $M_{200}-T_X$ relation in Arnaud et al. (2005).
[d] $M_{200,\text{X-lum}}$ estimated based on the $M_{200}-L_X$ relation in Leauthaud et al. (2010).
[e] The mean M_{200} estimated from $M_{200,\sigma}$, $M_{200,WL}$, and $M_{200,\text{X-temp}}$ (if available).

determinations by measuring the scatter in the best-fit estimates made by randomly selecting half the background galaxies as targets and repeating the fitting procedure for 500 sampled realizations.

In the weak lensing map, A2029 is obviously the most massive system ($M = (9.6 \pm 1.8) \times 10^{14}M_\odot$). The weak lensing mass estimate for A2033 is $(2.4 \pm 1.6) \times 10^{14}M_\odot$, and the mass estimate for SIG is $(1.3 \pm 1.5) \times 10^{14}M_\odot$. These mass estimates are smaller than the masses inferred from the $M_{200}-\sigma_{cl}$ relation. Interestingly, the estimated mass based on the weak lensing profile of SIG is smaller than the mass of A2033. Gonzalez et al. (2018) measured the masses of A2029 and A2033 based on an NFW fit to their weak lensing map. Their mass estimate for A2029 ($M = (9.1 \pm 5.6) \times 10^{14}M_\odot$) is consistent with ours. Their mass estimate for A2033 ($M = (6.5 \pm 4.0) \times 10^{14}M_\odot$) is somewhat larger than ours, but the uncertainty is also large, and they are thus consistent within the errors.

We obtain the X-ray properties from the *ROSAT* and *Chandra* data. Average temperature measurements were obtained using X-ray spectral fitting of the *Chandra* data for A2029 (ObsIDs: 892, 4977, 6101) and A2033 (ObsID: 15167). The *Chandra* data were reduced using the latest version of CIAO (version 4.10) with spectra extracted using the tool DMEXTRACT and response files created using MKWARF and MKACISRMF. The X-ray fitting was performed using XSPEC with an absorbed APEC model (Smith et al. 2001). To obtain the X-ray luminosities of A2029, A2033, SIG, and LOS1–12, we used the growth-curve analysis method described in Böhringer et al. (2013).

A2029 is very bright in the X-ray with a luminosity of ergs^{-1} and an X-ray temperature of $\sim$7.5 keV (Ebeling et al. 1998; Walker et al. 2012). A2033 is much fainter than A2029; the X-ray luminosity is erg s^{-1} and the temperature is 3.7 keV. The X-ray temperature we derive for A2033 is $\sim$1 keV lower than the previous measurement quoted in the BCS catalog (Ebeling et al. 1998). We also note that the X-ray temperature for A2033 is not in Gonzalez et al. (2018).

The X-ray morphology of SIG is disturbed, and there are some X-ray point sources that contaminate the X-ray emission. We measure the X-ray luminosity after subtracting the X-ray point sources; the X-ray luminosity of SIG is then $(1.57 \pm 0.05) \times 10^{43}$ erg s^{-1}. This X-ray luminosity is only $\sim$40% of the luminosity estimated from the flux listed in the second *ROSAT* PSPC source catalog (Rosat 2000). We are not able to estimate the temperature of SIG due to its low flux.
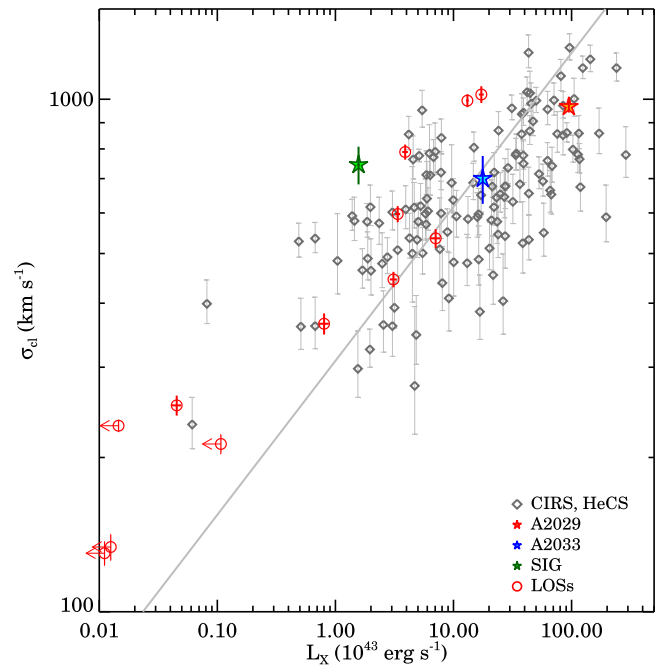

Figure 9. Velocity dispersion (σ_{cl}) vs. X-ray luminosity (L_X) for A2029 (red star), A2033 (blue star), and SIG (green star). The red circles display the foreground and background systems in the A2029 field. The red circles with arrows are the systems where we measure only the X-ray upper limits. The gray diamonds show the CIRS (Rines & Diaferio 2006) and HeCS (Rines et al. 2013) cluster samples. The solid line is the best-fit relation for nearby X-ray cluster samples from Zhang et al. (2011).

Figure 9 displays the velocity dispersion versus rest-frame X-ray luminosity within 0.1–2.4 keV for A2029, A2033, and SIG. We also include the foreground and background systems in the A2029 field. For comparison, we add cluster samples from Rines & Diaferio (2006) and Rines et al. (2013). The solid line in Figure 9 shows the scaling relation for local clusters from Zhang et al. (2011).

Here A2029 and A2033 follow the $L_X-\sigma_{cl}$ relation defined by previous cluster samples. SIG has a large velocity dispersion compared to the systems with similar X-ray luminosities, but it still follows the $L_X-\sigma_{cl}$ relation within the velocity dispersion uncertainty. The scaling relation for all of the systems in the A2029 field is consistent with the local scaling relation. This consistency is a strong check of the combined analysis we present.

We derive $M_{200,X}$ from the X-ray temperatures and luminosities of A2029, A2033, and SIG. We first compute

the $M_{200,Xtemp}$ of A2029 and A2033 based on the scaling relation of Arnaud et al. (2005),

$$M_{200,\text{X-temp}} = (5.74 \pm 0.3)$$
$$\times 10^{14} \left(\frac{kT}{5\text{ keV}}\right)^{(1.49 \pm 0.17)} \Big/ E(z)^{1/2}, \quad (2)$$

where $E(z) = [\Omega_m(1+z)^3 + (1 - \Omega_m)]$. The $M_{200,\text{X-temp}}$ of A2029 is $(10.25 \pm 0.85) \times 10^{14}M_\odot$ (Walker et al. 2012), and the $M_{200,\text{X-temp}}$ of A2033 is $(3.58 \pm 0.11) \times 10^{14}M_\odot$. The $M_{200,\text{X-temp}}$ of A2029 is comparable with the A2029 mass estimate from Ettori et al. (2018), $M_{200,\text{X-COP}} = (12.57 \pm 0.59) \times 10^{14}M_\odot$, who measured the hydrodynamic mass profile derived from the X-COP project. The mass estimates of A2029 and A2033 based on X-ray temperatures are close to their mass estimates based on both velocity dispersion and weak lensing.

Next, we derive $M_{200,\text{X-lum}}$ using the scaling relation between M_{200} and L_X from Leauthaud et al. (2010). The $M_{200,X}$ of A2029 is $(1.75 \pm 0.08) \times 10^{15}M_\odot$, a factor of two larger than the more robust mass estimates based on caustic and X-ray temperature profiles (Walker et al. 2012). Thus, the masses derived for A2033 and SIG from the $M_{200}–L_X$ relation, even though they are widely used, must be regarded with some caution. The M_{200} values of A2033 and SIG are $(5.14 \pm 0.59) \times 10^{14}M_\odot$ and $(0.32 \pm 0.02) \times 10^{14}M_\odot$, respectively. We convert M_{200} values into R_{200} values using the relation $M_{200} = 200\rho_{\text{crit}}(z)(4\pi/3)R_{200}^3$. The dashed circles in Figure 5(a) display the derived R_{200} values.

Table 4 summarizes all of the mass estimates for A2029, A2033, and SIG based on the various proxies. For A2029, only the mass estimate based on the X-ray luminosity disagrees with the other mass estimates. The mass estimates of A2033 from velocity dispersion, weak lensing, and X-ray temperature agree within 1σ. Again, the $M_{200,\text{X-lum}}$ of A2033 is larger than the other mass estimates. For SIG, the mass estimates based on weak lensing and X-ray luminosity are comparable. The larger offset of BGG with respect to the group mean redshift suggests that the large $M_{200,\sigma}$ of SIG is unreliable. In the following, we use the mean of the mass estimates based on velocity dispersion, weak lensing, and X-ray temperature (if available). We do not include the mass estimate based on the X-ray luminosity because it deviates substantially for the best-determined cases, A2029 and A2033.

5.2. Accretion of the Infalling Groups

To estimate the future accretion time of A2033 and SIG by A2029, we apply a two-body model separately for the orbits of A2033 and SIG relative to A2029 (Beers et al. 1982). This model computes a linear orbit for the system, assuming there is no shear or net rotation. Following Beers et al. (1982), we assume that A2033, SIG, and A2029 are at zero separation at $t = 0$ and now moving away or approaching each other for the first time in their history. The equation of motion for this system is

$$R = \frac{R_p}{\cos \alpha} = \frac{R_m}{2}(1 - \cos \chi), \quad (3)$$

$$V = \frac{V_r}{\sin \alpha} = \left(\frac{2GM}{R_m}\right)^{1/2} \frac{\sin \chi}{(1 - \cos \chi)}, \quad (4)$$

$$t = \left(\frac{R_m^3}{8GM}\right)^{1/2} (\chi - \sin \chi), \quad (5)$$

where R_p is the projected distance from the main cluster and the substructure, α is a projection angle between the plane of the sky and the line connecting two systems, R_m is the separation of the systems at maximum expansion, χ is the development angle, V_r is the relative radial velocity difference of the two systems, and M is the total mass of the system.

To solve the equation of motion, we use the observed R_p and V_r for the two groups: $R_p = 3.17$ Mpc and $V_r = 704.5$ km s^{-1} for A2033 and $R_p = 2.49$ Mpc and $V_r = 484.9$ km s^{-1} for SIG. We use the dynamical mass of A2029 measured from the caustic and the X-ray temperature profile, i.e., $M_{200} = 8.47 \times 10^{14}M_\odot$, and the masses of A2033 and SIG derived from their X-ray luminosities. When we solve the equation, we use the sum of the A2029 mass and the mass of either A2033 or SIG. We also set $t = 12.8$ Gyr, the age of the universe at the redshift of the cluster. We solve the equation of motion by increasing χ from 0 to 2π.

Figure 10 shows the projection angle (α) as a function of the radial velocity difference (V_r) of A2033 and SIG. We first plot the Newtonian criterion for gravitational binding (Beers et al. 1982):

$$V_r^2 R_p \leqslant 2GM_{\text{tot}} \sin^2 \alpha \cos \alpha. \quad (6)$$

This criterion divides the gravitationally bound (open) and unbound (shaded) regions in Figure 10.

By solving the equation of motion, we obtain a bound-outgoing solution for A2033. According to this bound-outgoing solution, A2033 is now at $\sim$13.5 Mpc from A2029 and moves away with a velocity of $V \sim 725$ km s^{-1}. This solution coincides with the result from Gonzalez et al. (2018). Considering the uncertainty in the mass estimates of the groups and the mean redshift measurements, there are also bound-incoming solutions (open circles in Figure 10(a)). For example, if we take the maximum total mass of this system, A2033 is approaching A2029 at $V \sim 842$ or 1214 km s^{-1}. In these case, A2033 collides with A2029 within $\sim$5.52 or $\sim$2.84 Gyr, respectively.

We also derive one bound-outgoing and two bound-incoming solutions for the A2029-SIG system. The bound-outgoing solution proposes that SIG is moving away at $V \sim 497$ km s^{-1} at a distance of $\sim$11.5 Mpc. The bound-incoming solutions suggest that SIG is approaching A2029 at $V \sim 581$ or 1111 km s^{-1}. The estimated collisional timescale for each case is $\sim$7.59 or $\sim$2.43 Gyr, respectively. The relative probability (p_i) of these solutions is

$$p_i = \int_{\alpha_{\inf,i}}^{\alpha_{\text{sup},i}} \cos \alpha \, d\alpha, \quad (7)$$

where $\alpha_{\text{sup},i}$ and $\alpha_{\inf,i}$ are computed by taking into account the uncertainties in the total mass of the system and the radial velocity difference. Then, the relative probabilities are normalized by $\sum(p_i)$. In the case of SIG, the probability that it is now incoming is $\sim$94%. Table 5 summarizes these solutions.

The detailed dynamics of the multicomponent A2029 system is probably much more complicated. The two-body model provides a guide to the timescales in the problem that complements the fact that the groups lie within the
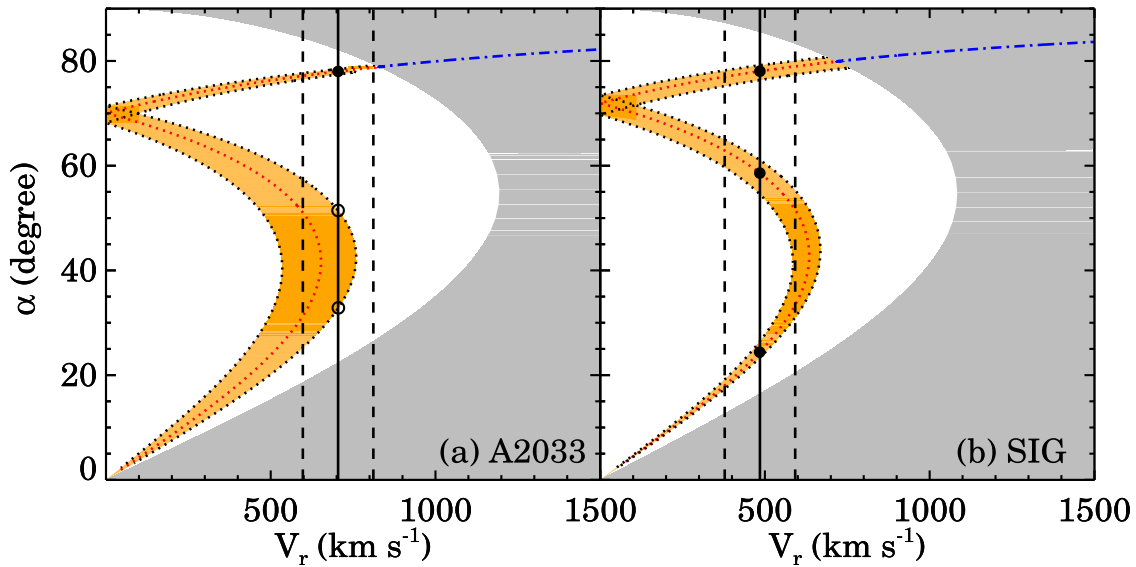
Figure 10. (a) Projection angle (α) vs. radial velocity difference (V_r) of A2033 given by the simple two-body model with $M_{tot} = 8.47 \times 10^{14}\ M_\odot$ of A2029 (Sohn et al. 2017). The vertical solid and dashed lines show the radial velocity differences and their 1σ uncertainties. The open and shaded regions indicate the gravitationally bound and unbound regions derived by the Newtonian criterion. The dotted and dot-dashed lines plot the bound and unbound solutions, respectively. The orange shaded regions indicate the uncertainty in the bound solutions originating from the mass estimate uncertainties. The filled circles indicate the solutions summarized in Table 5. (b) Same as (a) but for SIG.

Table 5
Two-body Model Solutions

Substructure	R_p (Mpc)	V_r (km s^{-1})	Solution	χ (rad)	α (deg)	R (Mpc)	R_{max} (Mpc)	V (km s^{-1})	t_{scl} (Gyr)	P (%)
A2033	3.17	704.5	Bound-outgoing	1.22	78.00	15.26	46.72	720.3	20.70	100
A2033			Bound-incoming[a]	4.27	48.16	4.75	6.66	841.5	5.52	…
A2033			Bound-incoming[a]	4.60	25.94	3.53	6.33	1214.6	2.84	…
SIG	2.49	484.9	Bound-outgoing	1.80	78.05	12.02	19.66	495.5	23.71	5
SIG			Bound-incoming	4.70	24.39	2.73	5.40	1171.8	2.28	68
SIG			Bound-incoming	4.08	58.59	4.78	5.99	567.7	8.23	26

Note.
[a] The bound-incoming solutions for the A2029–A2033 system are obtained by assuming the maximum total mass of this system.

caustics. The probability is roughly $\sim$70% of a merger in the next 3 Gyr (e.g., one of the bound-incoming solutions for SIG).

5.3. The Long-term Future Accretion for the A2029 System

The mass contained within the infalling groups constrains future mass accretion by A2029. To place A2029 in the context of other accreting systems, we consider the study by Haines et al. (2018), who identified *XMM*-detected X-ray groups in the infall region of 23 massive clusters at $z \sim 0.2$. They calculated the masses of infalling groups using the M_{200}–L_X relation (Leauthaud et al. 2010). The average mass retained in infalling groups per cluster is $2.23 \times 10^{14}\ M_\odot$, corresponding to $\sim$19% of the average M_{200} of the primary cluster. Because they identify infalling groups within $0.4 \leqslant R_{cl}/R_{200} \leqslant 1.3$, Haines et al. (2018) used the Millennium Simulation to correct the mass retained in infalling groups outside their survey region. They concluded that clusters accrete 16.2% $\pm$ 4.2% of their mass between $z = 0.223$ and the present day. Depending

primarily on the simulations (Zhao et al. 2009; Fakhouri et al. 2010; van den Bosch et al. 2014), they also suggested that groups contain only half of the expected total mass accreted by clusters.

The sum of the masses of the infalling groups, A2033 and SIG, is (6.0 $\pm$ 1.7) $\times 10^{14}\ M_\odot$, or $\sim$61% $\pm$ 19% of the A2029 mass, significantly larger than the measurements for the higher-redshift clusters. If we use the mass estimates of A2029, A2033, and SIG based on the M_{200}–L_X relation for direct comparison with Haines et al. (2018), the mass fraction within the infalling group is still large ($\sim$31% $\pm$ 4%). We note that this mass fraction is a lower limit because it does not account for the rest of the mass contained within the infall region.

Because A2033 and SIG lie comfortably within the caustics and the two-body model has only bound solutions including several inbound trajectories, all infalling groups should eventually be accreted onto A2029, implying a high accretion rate compared to the measurements from $z \sim 0.22$ clusters (Haines et al. 2018). The growth rate also significantly exceeds expectations based on numerical simulations. For example, the

growth rate of a massive dark matter halo with $10^{15} M_\odot$ derived from the Millennium-II simulation (Equation (2) in Fakhouri et al. 2010) is $\sim 1.1 \times 10^{14} M_\odot$ (11% of the dark matter halo mass) from the A2029 redshift ($z \sim 0.08$, ~ 1 Gyr look-back time) to the present day. A2029 suggests that stochastic variations in the accretion rate are large.

The caustic method we use for identifying cluster members provides a mass profile of the cluster often extending to the turnaround radius (Diaferio & Geller 1997; Diaferio 1999). Based on the mass profile from the A2029 caustics, we estimate the mass retained within the entire infall region. First, we consider a spherical shell with inner and outer radii of 1.99 and 3.66 Mpc, respectively, 500 kpc smaller than the distance to SIG from the A2029 core and 500 kpc larger than the distance to A2033 from the A2029 core. The mass within this spherical shell is $4.93^{+1.24}_{-1.24} \times 10^{14} M_\odot$, comparable with the sum of the masses of A2033 and SIG estimated from the $M_{200}-L_X$ relation. The systematic uncertainties in the masses of A2033 and SIG are large (Table 4): the two systems contain at least half of the mass in this annulus, and they probably dominate the mass.

The caustic mass profile, which was not treated by Gonzalez et al. (2018), also provides an estimate of the ultimate halo mass of A2029 (Rines et al. 2013). Simulations demonstrate that most of the mass ($\sim 90\%$) within a radius enclosing an overdensity of $\sim 5.6 \rho_{crit}$ is ultimately accreted by the halo (Busha et al. 2005; Dünner et al. 2006). We refer to this mass as the ultimate mass of the cluster. Rines et al. (2013) estimated the ultimate masses of 58 clusters ($M_{5.6}$) and demonstrated that the typical ratio between the M_{200} and the ultimate mass is $\sim 1.99 M_{200}$. The ultimate mass of A2029 is $M_{5.6} = 1.58^{+5.04}_{-4.98} \times 10^{15} M_\odot$, or $(1.86 \pm 0.36) M_{200}$. This result is completely consistent with that of Rines et al. (2013). In summary, the current A2029 contains 54% of the ultimate halo mass, A2033 and SIG contain $34\% \pm 12\%$ of the ultimate halo mass, and the remainder is distributed throughout the infall region, possibly in lower-mass groups (mostly at radii larger than $R_{cl} > 3.7$ Mpc).

The large mass accretion rate of A2029 is interesting but may not be surprising because it is one of the most massive clusters in the nearby universe. The accretion rate as a function of cluster mass and redshift is a powerful constraint on the hierarchical growth of these systems. Even with the extensive data set for A2029, the uncertainties in the dynamical future of the system remain large. Having a comprehensive observational view of the system extending throughout the infall region is crucial for estimating the ultimate mass of the system. All of the data taken together suggest that A2029 experienced an accretion event 3 Gyr ago and will experience one or more events within the next 3 Gyr.

6. Summary

We combine a dense redshift survey of the local massive cluster A2029 with X-ray and weak lensing maps to elucidate a comprehensive model of the future accretion story of this massive system. The total data set for A2029 is unusually rich. The redshift survey is essentially complete within a wide field of $R_{cl} < 40'(=3.5$ Mpc) around A2029. We refine the analysis of the *ROSAT* images and the weak lensing map to improve the mass estimated for two massive subsystems, A2033 and SIG, within the A2029 infall region.

The infalling groups, A2033 and SIG, appear in the weak lensing map, X-ray image, and spectroscopic survey.

Interestingly, the brightest galaxies in these subgroups are offset from the group centers (determined by X-ray or cluster members). The astrophysical implications of these offsets are unclear.

The complete redshift survey facilitates the identification of newly identified foreground and background groups in the A2029 field. This identification is critical for removing spurious contributions to the mass within the infall region. We identify at least 12 foreground/background systems. Among these systems, 10 have *ROSAT* X-ray counterparts; a very bright X-ray group, LOS7, lies at $z = 0.223$. Oddly, its position makes it appear to be a filamentary connection between A2033 and A2029. The redshift survey makes it clear that this apparent connection is merely a superposition. Taking these extended X-ray sources together with A2029, A2033, and SIG, we demonstrate that they are all consistent with the well-known scaling relation between X-ray luminosity and velocity dispersion.

We measure the mass of A2029 based on the three different mass proxies: caustics, weak lensing, and X-ray luminosity (or temperature). The caustic mass based on the spectroscopic members is $M_{200} = (8.47 \pm 0.25) \times 10^{14} M_\odot$ and agrees to within 1σ with the X-ray estimate. We also estimate the masses of infalling groups using velocity dispersions, weak lensing, and X-ray luminosities. Within the much larger uncertainties, the estimates agree. They imply that the total mass in these two subsystems is $\sim 60\%$ of the mass of the main cluster.

A simple two-body model traces the future accretion of the infalling groups. The model suggests that the infalling groups are obviously bound to A2029 and may be accreted by the primary cluster within ~ 3 Gyr. This accretion rate is larger than the average predicted by the simulations.

The infall region as a whole contains an amount of mass comparable with the A2029 M_{200}. The two massive subsystems contribute $\sim 60\%$ of the mass in the infall region. Numerical simulations suggest that 90% of the mass in the infall region will be accreted in the long-term future of the cluster.

In the future, a combination of eROSITA, PFS, and Euclid observations will make similar analyses possible for clusters across a broad range of cluster mass and over a wide redshift range. These combined spectroscopic, X-ray, and weak lensing observations will enable construction of the full picture of the accretion story of clusters of galaxies. They will provide a strong test of the hierarchical structure formation picture.

Appendix
Spectroscopically Identified Stars in the A2029 Field

We identify 97 stars in the A2029 field from our spectroscopic survey. These objects are either stars with SDSS spectroscopic redshifts or Hectospec targets that were classified as galaxies based on the SDSS algorithm. These stars have absolute radial velocities smaller than $500\,\mathrm{km\,s^{-1}}$. For completeness, we provide a catalog of these stars in the A2029 field, including SDSS object ID, R.A., decl., r-band magnitude, and redshift (or blueshift) and its uncertainty (Table 6).

Table 6
The Catalog of Stars in the A2029 Field

SDSS Object ID	R.A.	Decl.	$r_{\mathrm{cModel,0}}$	z
1237658780557836343	227.727719	5.757971	19.99	-0.00008 ± 0.00009
1237655744020021696	227.711226	5.716711	20.80	-0.00065 ± 0.00016
1237655744020086825	227.778066	5.722604	15.20	-0.00001 ± 0.00014
1237655744020086971	227.742827	5.697524	16.40	-0.00018 ± 0.00003
1237662268074033278	227.833153	5.788820	15.33	0.00003 ± 0.00004
1237662268074033279	227.835948	5.790469	15.28	-0.00014 ± 0.00004
1237655744020086887	227.848296	5.668711	19.76	-0.00011 ± 0.00014
1237658780557770986	227.669673	5.830535	16.44	-0.00000 ± 0.00007
1237662268074034025	227.788274	5.871173	20.60	-0.00034 ± 0.00013
1237655744020021260	227.609299	5.665744	16.43	-0.00007 ± 0.00004

(This table is available in its entirety in machine-readable form.)

ORCID iDs

Jubee Sohn ⬥ https://orcid.org/0000-0002-9254-144X
Margaret J. Geller ⬥ https://orcid.org/0000-0002-9146-4876
Stephen A. Walker ⬥ https://orcid.org/0000-0001-8831-2073

References

Abell, G. O., Corwin, H. G., Jr., & Olowin, R. P. 1989, ApJS, 70, 1
Alam, S., Albareti, F. D., Allende Prieto, C., et al. 2015, ApJS, 219, 12
Amendola, L., Appleby, S., Avgoustidis, A., et al. 2018, LRR, 21, 2
Arnaud, M., Pointecouteau, E., & Pratt, G. W. 2005, A&A, 441, 893
Beers, T. C., Geller, M. J., & Huchra, J. P. 1982, ApJ, 257, 23
Benítez, N. 2000, ApJ, 536, 571
Böhringer, H., Chon, G., Collins, C. A., et al. 2013, A&A, 555, A30
Bond, J. R., Kofman, L., & Pogosyan, D. 1996, Natur, 380, 603
Bower, R. G., Ellis, R. S., & Efstathiou, G. 1988, MNRAS, 234, 725
Boylan-Kolchin, M., Springel, V., White, S. D. M., Jenkins, A., & Lemson, G.
    2009, MNRAS, 398, 1150
Busha, M. T., Evrard, A. E., Adams, F. C., & Wechsler, R. H. 2005, MNRAS,
    363, L11
Clarke, T. E., Blanton, E. L., & Sarazin, C. L. 2004, ApJ, 616, 178
Colberg, J. M., Krughoff, K. S., & Connolly, A. J. 2005, MNRAS, 359, 272
Danese, L., de Zotti, G., & di Tullio, G. 1980, A&A, 82, 322
De Boni, C., Serra, A. L., Diaferio, A., Giocoli, C., & Baldi, M. 2016, ApJ,
    818, 188
Diaferio, A. 1999, MNRAS, 309, 610
Diaferio, A., & Geller, M. J. 1997, ApJ, 481, 633
Dünner, R., Araya, P. A., Meza, A., & Reisenegger, A. 2006, MNRAS, 366, 803
Ebeling, H., Edge, A. C., Bohringer, H., et al. 1998, MNRAS, 301, 881
Eckert, D., Ettori, S., Pointecouteau, E., et al. 2017, AN, 338, 293
Erben, T., Van Waerbeke, L., Bertin, E., Mellier, Y., & Schneider, P. 2001,
    A&A, 366, 717
Ettori, S., Ghirardini, V., Eckert, D., et al. 2018, arXiv:1805.00035
Fabricant, D., Fata, R., Roll, J., et al. 2005, PASP, 117, 1411
Fakhouri, O., & Ma, C.-P. 2008, MNRAS, 386, 577
Fakhouri, O., Ma, C.-P., & Boylan-Kolchin, M. 2010, MNRAS, 406, 2267
Geller, M. J., Diaferio, A., & Kurtz, M. J. 1999, ApJL, 517, L23
Geller, M. J., Diaferio, A., Rines, K. J., & Serra, A. L. 2013, ApJ, 764, 58
Giocoli, C., Tormen, G., & Sheth, R. K. 2012, MNRAS, 422, 185
Gonzalez, E. J., de los Rios, M., Oio, G. A., et al. 2018, A&A, 611, A78
Haines, C. P., Finoguenov, A., Smith, G. P., et al. 2018, MNRAS, arXiv:1709.
    04945
Hao, J., McKay, T. A., Koester, B. P., et al. 2010, ApJS, 191, 254
Hoekstra, H., Hartlap, J., Hilbert, S., & van Uitert, E. 2011, MNRAS, 412, 2095
Hwang, H. S., Geller, M. J., Diaferio, A., Rines, K. J., & Zahid, H. J. 2014,
    ApJ, 797, 106
Kaiser, N. 1987, MNRAS, 227, 1
Kurtz, M. J., & Mink, D. J. 1998, PASP, 110, 934
Lauer, T. R., Postman, M., Strauss, M. A., Graves, G. J., & Chisari, N. E. 2014,
    ApJ, 797, 82
Leauthaud, A., Finoguenov, A., Kneib, J.-P., et al. 2010, ApJ, 709, 97

Lewis, A. D., Stocke, J. T., & Buote, D. A. 2002, ApJL, 573, L13
Liu, A., Yu, H., Diaferio, A., et al. 2018, arXiv:1806.10864
Martinet, N., Clowe, D., Durret, F., et al. 2016, A&A, 590, A69
McBride, J., Fakhouri, O., & Ma, C.-P. 2009, MNRAS, 398, 1858
McCleary, J., dell'Antonio, I., & Huwe, P. 2015, ApJ, 805, 40
McCleary, J., dell'Antonio, I., & von der Linden, A. 2018, arXiv:1812.08356
Merloni, A., Predehl, P., Becker, W., et al. 2012, arXiv:1209.3114
Neto, A. F., Gao, L., Bett, P., et al. 2007, MNRAS, 381, 1450
Okabe, N., Okura, Y., & Futamase, T. 2010, ApJ, 713, 291
Patel, P., Maddox, S., Pearce, F. R., Aragón-Salamanca, A., & Conway, E.
    2006, MNRAS, 370, 851
Paterno-Mahler, R., Blanton, E. L., Randall, S. W., & Clarke, T. E. 2013, ApJ,
    773, 114
Regos, E., & Geller, M. J. 1989, AJ, 98, 755
Reisenegger, A., Quintana, H., Carrasco, E. R., & Maze, J. 2000, AJ, 120, 523
Rines, K., & Diaferio, A. 2006, AJ, 132, 1275
Rines, K., Geller, M. J., Diaferio, A., et al. 2002, AJ, 124, 1266
Rines, K., Geller, M. J., Diaferio, A., & Kurtz, M. J. 2013, ApJ, 767, 15
Rosat, C. 2000, yCat, 9030, 0
Sarazin, C. L., Wise, M. W., & Markevitch, M. L. 1998, ApJ, 498, 606
Schirmer, M., Erben, T., Schneider, P., Wolf, C., & Meisenheimer, K. 2004,
    A&A, 420, 75
Schneider, P. 1996, MNRAS, 283, 837
Serra, A. L., & Diaferio, A. 2013, ApJ, 768, 116
Serra, A. L., Diaferio, A., Murante, G., & Borgani, S. 2011, MNRAS, 412,
    800
Sifón, C., Hoekstra, H., Cacciato, M., et al. 2015, A&A, 575, A48
Smith, R. K., Brickhouse, N. S., Liedahl, D. A., & Raymond, J. C. 2001, ApJL,
    556, L91
Snowden, S. L., McCammon, D., Burrows, D. N., & Mendenhall, J. A. 1994,
    ApJ, 424, 714
Sohn, J., Geller, M. J., Zahid, H. J., et al. 2017, ApJS, 229, 20
Sohn, J., Hwang, H. S., Geller, M. J., et al. 2015, JKAS, 48, 381
Szabo, T., Pierpaoli, E., Dong, F., Pipino, A., & Gunn, J. 2011, ApJ, 736, 21
Takada, M., Ellis, R. S., Chiba, M., et al. 2014, PASJ, 66, R1
Tyler, K. D., Rieke, G. H., & Bai, L. 2013, ApJ, 773, 86
Umetsu, K., & Diemer, B. 2017, ApJ, 836, 231
Uson, J. M., Boughn, S. P., & Kuhn, J. R. 1991, ApJ, 369, 46
van den Bosch, F. C. 2002, MNRAS, 331, 98
van den Bosch, F. C., Jiang, F., Hearin, A., et al. 2014, MNRAS,
    445, 1713
von der Linden, A., Allen, M. T., Applegate, D. E., et al. 2014, MNRAS, 439, 2
Walker, S. A., Fabian, A. C., Sanders, J. S., George, M. R., & Tawara, Y. 2012,
    MNRAS, 422, 3503
Wen, Z. L., Han, J. L., & Liu, F. S. 2009, ApJS, 183, 197
Wen, Z. L., Han, J. L., & Liu, F. S. 2012, ApJS, 199, 34
Yu, H., Diaferio, A., Agulli, I., Aguerri, J. A. L., & Tozzi, P. 2016, ApJ,
    831, 156
Yu, H., Diaferio, A., Serra, A. L., & Baldi, M. 2018, ApJ, 860, 118
Yu, H., Serra, A. L., Diaferio, A., & Baldi, M. 2015, ApJ, 810, 37
Zhang, Y.-Y., Andernach, H., Caretta, C. A., et al. 2011, A&A, 526, A105
Zhao, D. H., Jing, Y. P., Mo, H. J., & Börner, G. 2009, ApJ, 707, 354
ZuHone, J. A., Markevitch, M., & Johnson, R. E. 2010, ApJ, 717, 908